Wrinkling and folding analysis of elastic membranes using an enhanced rotation-free thin shell triangular element

Fernando G. Flores [a], Eugenio Oñate [b],*

[a] Department of Structures, National University of Córdoba, P.O. Box 916, 5000 Córdoba, Argentina
[b] International Center for Numerical Methods in Engineering (CIMNE), Technical University of Catalonia, Campus Norte UPC, 08034 Barcelona, Spain

ABSTRACT

This paper presents a formulation for analysis of thin elastic membranes using a rotation-free shell element within an explicit time integration strategy. The applications presented are isotropic/anisotropic rectangular membranes under shear forces and fabric drapes falling over a pedestal. Results are compared with other numerical results existing in the literature.

© 2011 Elsevier B.V. All rights reserved.

1. Introduction

The design of membranes for different applications like thin films, solar sails or many textile applications relies strongly on computer simulations. Thin films and textile fabrics easily wrinkle or fold in the presence of low compressive stresses due to the low bending stiffness.

Traditionally the wrinkling phenomena are analyzed with tension field theory and modeled with membrane elements endowed with a special kinematic or constitutive law that precludes compression. The main limitation of these approaches is that they do not provide the detailed wrinkled configuration. A comprehensive overview of the work carried out on tension field theory until 1990 can be found in [1] and references cited therein. There are a large number of papers in the literature using different techniques to introduce the non-compression behavior in membranes elements. To mention just a few recent papers, Raible et al. [2] developed a wrinkling algorithm for orthotropic membrane materials based on a split of the deformation tensor. Akita et al. [3] presented a projection technique to obtain a modified plane stress elasticity matrix. This later model was extended in Ref. [4] exploiting the elasto-plasticity concept making it also applicable for both isotropic and orthotropic

materials. Pagitz and Abdalla presented a multi-grid approach including an in-plane rotational DOF that defines wrinkle direction [5]. Wrinkling of inelastic membranes has been considered by Mosler and Cirak [6]. To capture the detailed geometry of wrinkles Weinberg and Neff [7] proposed a geometrically exact thin membrane model including rotational DOFS and introducing an artificial viscosity.

In general if the detailed configuration is desired, the simulation must account for both membrane and bending effects, i.e. shell elements are necessary. Besides that, due to a low elastic shear modulus a full non-linear kinematic model for moderate strains (including anisotropic behavior for fabrics) must be used. The main aspects of the problem at hand may be summarized as follows (see also Ref. [8] for fundamental aspects of thin shell analysis including many examples):

- Kirchhoff–Love hypothesis for shell analysis are reasonable.
- Bending stiffness is very low but necessary to obtain: (a) size and number of wrinkles and (b) detailed deformed 3D shapes.
- Fine discretizations may be needed.
- Large displacements and rotations must be considered.
- Anisotropic behavior with moderate strains must be accounted for.

The use of standard shell elements, i.e. based on C° continuity requirements, may have problems due to the transverse shear approaches commonly used. In the last decade an important number of elements based on classical shell theory (i.e. neglecting transverse

shear strains) have been proposed. All these approximations are non-conforming and do not include rotation degrees of freedom (DOFs). Most of the approximations compute the curvatures resorting to a patch of elements and can be seen as a finite difference generalization on an arbitrary triangular mesh, see for example [9–12]. These elements have been extended in different ways including branching shells [13], orthotropic materials [14,15] and textile composites [16]. Other approaches include the use of subdivision surfaces [17] or discontinuous Galerkin methods [18]. Three of the main advantages of rotation-free elements over standard elements are (a) as rotation DOFs are not included, the total number of degrees of freedom is drastically reduced (typically to 50% or 60%) with important savings in both storage and CPU time, (b) problems associated with rotation vectors or local triads (non-symmetric matrices for instance) that are in general costly and difficult to parameterize and update do not appear, and (c) no special techniques are necessary to deal with problems appearing in the thin shell limit (e.g. shear locking). Some drawbacks also exist, we can mention: (a) sensitivity to irregular nodes (a regular node is one shared by six elements), (b) a direct combination with other finite elements, like beam or solid elements, is not straightforward and (c) coding may be more involved.

The large displacement static analysis of very thin shells (pseudo-membranes) requires special techniques as the problem is numerically sensitive. The main aspects to be considered and the problems that commonly appear in these simulations are (for implicit solvers):

- ill-conditioned stiffness matrix;
- special strategies may be needed due to null/negative stiffness (membrane and bending);
- large number of DOFs leading to large storage capacity needs;
- shear locking (when using a degenerated-solid approach or Mindlin-type elements);
- inclusion of geometric imperfections may be necessary to trigger buckling;
- contact and self-contact may be present (low order elements must be used);
- short steps and continuous reformulation of the stiffness matrix are needed;
- non-symmetric matrices may appear due to: (a) contact with friction and (b) local triads.

To circumvent some of the drawbacks listed above the finite element considered here is a "non-conforming" (both membrane and bending) rotation-free linear strain shell triangle resorting to a four-element patch to compute the membrane and bending strains [13]. Instead of using an implicit solver, pseudo-static solutions are obtained using an explicit integration of the damped momentum equations [19]. This strategy is similar to relaxation techniques, see for example [20,21]. This approach allows to easily dealing with the important instabilities associated with wrinkle formation. Geometric imperfections and initial stress states, typically introduced in implicit static solutions, are avoided. Self-weight or an initial velocity is introduced instead to trigger normal displacements.

The main targets of this paper are (a) to show that the linear strains rotation-free shell triangle presented is very adequate for analysis of thin membranes under a variety of conditions, (b) to show that very accurate solutions are obtained for complex wrinkling problems with rather coarse meshes, and (c) to demonstrate that explicit integrators do not require special strategies to deal with the low bending stiffness and the strong instabilities of membranes.

2. The enhanced basic shell triangle (EBST)

In this section, for the sake of completeness, a brief summary of the rotation-free shell triangle used in this work. More details can be found in the original references [10,13,22]. The starting point of the rotation-free so-called basic shell triangle (BST) is to discretize the shell surface with a standard three-node triangular mesh. The difference with a standard finite element method is that, for the computation of strains within an element, the configuration of the three adjacent triangular elements is also used. Then, at each triangle a, four-element-patch formed by the central triangle and the three adjacent ones is considered (see Fig. 1a).

In the original rotation-free BST element the displacement field was linearly interpolated from the nodal values within each triangle [9] leading to a constant membrane field. The curvature field over each triangular element was computed using information from the displacements of the three adjacent triangles [10]. In this work we use the enhanced basic shell triangle (EBST) formulation as described in [13]. The displacement field in the EBST element is interpreted quadratic for the nodal displacement values at the six nodes of the four-element patch of Fig. 1.

2.1. Membrane strains computation

We use a standard quadratic approximation of the shell geometry over the six-node patch of triangle (Fig. 1) as

$$\boldsymbol{\varphi} = \sum_{i=1}^{6} L^i \boldsymbol{\varphi}^i = \sum_{i=1}^{6} L^i (\boldsymbol{\varphi}_0^i + \mathbf{u}^i) \tag{1a}$$

where $\boldsymbol{\varphi}^i = [x_1^i, x_2^i, x_3^i]^T$ is the position vector of node i, $\boldsymbol{\varphi}_0^i$ is the position vector at the initial configuration, $\mathbf{u}^i = [u_1^i, u_2^i, u_3^i]^T$ is the
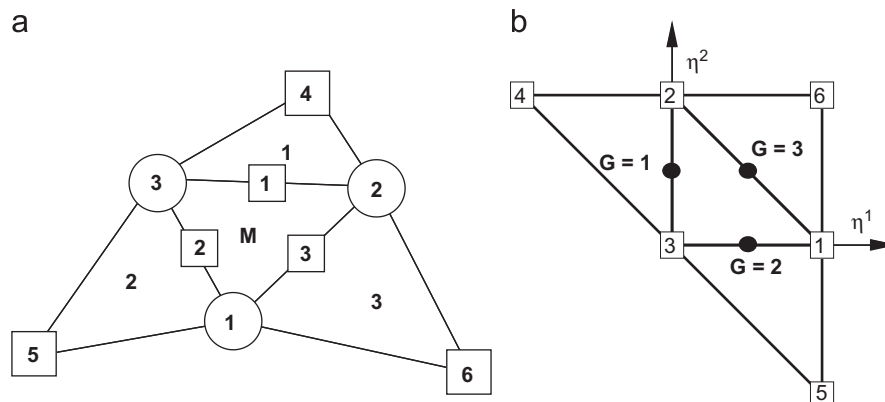

Fig. 1. Patch of triangles for computation of strains in the EBST element M.

displacement vector and

$$L^1 = \eta^1 + \eta^2\eta^3 \quad L^2 = \eta^2 + \eta^3\eta^1 \quad L^3 = \eta^3 + \eta^1\eta^2$$

$$L^4 = \frac{\eta^1}{2}(\eta^1 - 1) \quad L^5 = \frac{\eta^2}{2}(\eta^2 - 1) \quad L^6 = \frac{\eta^3}{2}(\eta^3 - 1) \tag{1b}$$

with η^1 and η^2 the natural coordinates (also area coordinates) in the parametric space (see Fig. 1b) and $\eta^3 = 1 - \eta^1 - \eta^2$.

Note in Fig. 1 that, as usual, for the numeration of the sides and the adjacent elements the opposite local node is used, and naturally the same numeration is used for the mid-side points *G*. Note also that the numeration of the rest of the nodes in the patch begins with the node opposite to local node 1, then each extra node and each mid-side point can be easily referenced.

From Eq. (1a) the gradient at each mid-side *G* point of the central triangle *M* with respect to a local in-plane Cartesian system $(x_1 - x_2)$ can be written as:

$$\begin{bmatrix} \boldsymbol{\varphi}_{,1} \\ \boldsymbol{\varphi}_{,2} \end{bmatrix}^{(I)} = \begin{bmatrix} L^1_{,1} & L^2_{,1} & L^3_{,1} & L^{I+3}_{,1} \\ L^1_{,2} & L^2_{,2} & L^3_{,2} & L^{I+3}_{,2} \end{bmatrix}^{(I)} \begin{bmatrix} \boldsymbol{\varphi}^1 \\ \boldsymbol{\varphi}^2 \\ \boldsymbol{\varphi}^3 \\ \boldsymbol{\varphi}^{I+3} \end{bmatrix} \tag{2}$$

Note that the gradient depends on the three nodes of the main element and (only) on the extra node $(I+3)$, associated to the side (I). This fact implies that a unique value will be obtained for the gradient when it is evaluated from any of the two neighbor elements. In Eq. (2) the super index surrounded by brackets indicate evaluated at the center of side *I*, while the super index on nodal shape functions and nodal coordinates indicate the node.

Defining the metric tensor at each mid-side point:

$$g^{(I)}_{\alpha\beta} = \boldsymbol{\varphi}^{(I)}_{,\alpha} \cdot \boldsymbol{\varphi}^{(I)}_{,\beta} \tag{3}$$

a linear interpolation can be defined over the element as

$$\mathbf{g}(\boldsymbol{\eta}) = (1 - 2\eta^1)\mathbf{g}^{(1)} + (1 - 2\eta^2)\mathbf{g}^{(2)} + (1 - 2\eta^3)\mathbf{g}^{(3)} \tag{4}$$

and any convenient Lagrangian strain measure **E** can be computed from it

$$\mathbf{E} = f(\mathbf{g}) \tag{5}$$

We note that the definition of **g** in Eq. (4) is equivalent to using a linear "assumed strain" approach [10,22].

In our case a unique point is used at the element center with the average of the metric tensors computed at mid-side points. This is equivalent to using one point quadrature for the assumed strain field:

$$\mathbf{g}(\boldsymbol{\eta}) = \frac{1}{3}(\mathbf{g}^{(1)} + \mathbf{g}^{(2)} + \mathbf{g}^{(3)}) \tag{6}$$

The element is then non-conforming. However, it satisfies the "patch test", and the approach can be used for large displacement problems [10].

2.2. Computation of curvatures

Curvatures will be assumed to be constant within each element. An averaging of the curvatures $\kappa_{\alpha\beta}$ is made over the element in a mean integral sense as

$$\kappa_{\alpha\beta} = \frac{-1}{A} \int_A \mathbf{t}_3 \cdot \boldsymbol{\varphi}_{,\beta\alpha} \, dA \tag{7}$$

Integrating by parts the right hand side of previous equation gives

$$\kappa_{\alpha\beta} = \frac{1}{A} \oint_\Gamma n_\alpha \, \mathbf{t}_3 \cdot \boldsymbol{\varphi}_{,\beta} \, d\Gamma \tag{8}$$

$$\begin{bmatrix} \kappa_{11} \\ \kappa_{22} \\ 2\kappa_{12} \end{bmatrix} = \frac{-1}{A} \oint_\Gamma \begin{bmatrix} n_1 & 0 \\ 0 & n_2 \\ n_2 & n_1 \end{bmatrix} \begin{bmatrix} \mathbf{t}_3 \cdot \boldsymbol{\varphi}_{,1} \\ \mathbf{t}_3 \cdot \boldsymbol{\varphi}_{,2} \end{bmatrix} d\Gamma \tag{9}$$

Adopting one-point integration on each side and using the standard area coordinates (η^i) derivatives we have

$$\begin{bmatrix} \kappa_{11} \\ \kappa_{22} \\ 2\kappa_{12} \end{bmatrix} = -2 \sum_{I=1}^{3} \begin{bmatrix} \eta^I_{,1} & 0 \\ 0 & \eta^I_{,2} \\ \eta^I_{,2} & \eta^I_{,1} \end{bmatrix} \begin{bmatrix} \boldsymbol{\varphi}_{,1} \cdot \mathbf{t}_3 \\ \boldsymbol{\varphi}_{,2} \cdot \mathbf{t}_3 \end{bmatrix}^{(I)} \tag{10}$$

where *A* is the element area and $\mathbf{t}_3$ is the average normal for the element, used as a reference direction. In this case $\mathbf{t}_3$ is simply taken as the normal to the central triangle *M*. The gradient $\boldsymbol{\varphi}_{,\alpha}$ at each mid-side point *G* is computed from Eq. (2). Other alternatives for computing $\boldsymbol{\varphi}_{,\alpha}$ are possible as discussed in [10]. For future use it is convenient to introduce the vectors:

$$\mathbf{h}_{\alpha\beta} = \sum_{I=1}^{3} (\eta^I_{,\alpha} \boldsymbol{\varphi}^{(I)}_{,\beta} + \eta^I_{,\beta} \boldsymbol{\varphi}^{(I)}_{,\alpha}) \tag{11}$$

The stretching of the shell in the normal direction is defined by a parameter λ as

$$\lambda = \frac{h}{h^0} = \frac{A^0}{A} \tag{12}$$

where *h* and h^0 are the actual and original thickness, respectively.

The second equality assumes that the deformation is isochoric (and elastic). The assumption that the fiber originally normal to the surface in the reference configuration is also normal to the surface in the current configuration (Kirchhoff hypothesis) is adopted herein.

2.3. Nodal force computation

The element is formulated for inelastic problems in the large strain range, but the applications shown below are all elastic and mainly in the small strain range. For completeness some details will be given regarding the computation of equivalent nodal forces under the hypothesis of small elastic strains. This allows considering separately membrane and bending stresses.

For membrane forces the Green–Lagrange strain tensor on the middle surface is used. This can be readily obtained from Eqs. (2), (3) and (6):

$$\mathbf{E}_{GL} = \frac{1}{2} \begin{bmatrix} g_{11} - 1 & g_{12} \\ g_{12} & g_{22} - 1 \end{bmatrix} \tag{13}$$

The membrane forces at the element center are computed using a linear orthotropic stress-strain relation in material coordinates (in Voigt's notation):

$$\mathbf{N} = \begin{bmatrix} N_{11} \\ N_{22} \\ N_{12} \end{bmatrix} = \begin{bmatrix} D^m_{11} & D^m_{12} & D^m_{13} \\ & D^m_{22} & D^m_{23} \\ symm. & & D^m_{33} \end{bmatrix} \begin{bmatrix} E_{11} \\ E_{22} \\ 2E_{12} \end{bmatrix} = \mathbf{D}^m \mathbf{E} \tag{14}$$

The membrane strains variation is

$$\delta \begin{bmatrix} E_{11} \\ E_{22} \\ 2E_{12} \end{bmatrix} = \frac{1}{3} \sum_{I=1}^{3} \sum_{J=1}^{4} \begin{bmatrix} L^{J(I)}_{,1} \boldsymbol{\varphi}^{(I)}_{,1} \cdot \delta \mathbf{u}^J \\ L^{J(I)}_{,2} \boldsymbol{\varphi}^{(I)}_{,2} \cdot \delta \mathbf{u}^J \\ L^{J(I)}_{,2} \boldsymbol{\varphi}^{(I)}_{,1} \cdot \delta \mathbf{u}^J + L^{J(I)}_{,1} \boldsymbol{\varphi}^{(I)}_{,2} \cdot \delta \mathbf{u}^J \end{bmatrix} = \mathbf{B}_m \delta \mathbf{a}^p \tag{15}$$

where for each mid-side point $(G=I)$ there are contributions from the four nodes (J). In Eq. (15) $\mathbf{B}_m$ is the membrane strain-displacement matrix and $\mathbf{a}^p$ is the patch displacement vector. The form of $\mathbf{B}_m$ can be found in [10,22].

For bending stresses a similar relation is written between moments and curvatures as

$$\mathbf{M} = \begin{bmatrix} M_{11} \\ M_{22} \\ M_{12} \end{bmatrix} = \begin{bmatrix} D_{11}^b & D_{12}^b & D_{13}^b \\ & D_{22}^b & D_{23}^b \\ symm. & & D_{33}^b \end{bmatrix} \begin{bmatrix} \kappa_{11} \\ \kappa_{22} \\ 2\kappa_{12} \end{bmatrix} = \mathbf{D}^b \boldsymbol{\kappa} \quad (16)$$

Curvature-displacement variations are more involved. The resulting expression is (see [10,22] for details)

$$\delta\boldsymbol{\kappa} = \delta \begin{bmatrix} \kappa_{11} \\ \kappa_{22} \\ 2\kappa_{12} \end{bmatrix} = 2\sum_{I=1}^{3} \begin{bmatrix} \eta_{/1}^I & 0 \\ 0 & \eta_{/2}^I \\ \eta_{/2}^1 & \eta_{/1}^I \end{bmatrix} \sum_{J=1}^{4} \begin{bmatrix} L_{/1}^{J(I)}(\mathbf{t}_3 \cdot \delta\mathbf{u}^J) \\ L_{/2}^{J(I)}(\mathbf{t}_3 \cdot \delta\mathbf{u}^J) \end{bmatrix}$$
$$-2\sum_{I=1}^{3} \begin{bmatrix} (\eta_{/1}^I \rho_{11}^1 + \eta_{/2}^I \rho_{11}^2) \\ (\eta_{/1}^I \rho_{22}^1 + \eta_{/2}^I \rho_{22}^2) \\ (\eta_{/1}^I \rho_{12}^1 + \eta_{/2}^I \rho_{12}^2) \end{bmatrix} (\mathbf{t}_3 \cdot \delta\mathbf{u}^I) = \mathbf{B}_b \delta\mathbf{a}^p \quad (17)$$

where the projections of the vectors $\mathbf{h}_{\alpha\beta}$ over the contravariant base vectors $\tilde{\boldsymbol{\varphi}}_{/\alpha}$ have been included:

$$\rho_{\alpha\beta}^\delta = \mathbf{h}_{\alpha\beta} \cdot \tilde{\boldsymbol{\varphi}}_{/\delta} \quad (18)$$

The form of the bending strain matrix $\mathbf{B}_b$ can be found in [10,22].

Finally, the equivalent nodal forces at element level ($\mathbf{r}^e$) can be computed as:

$$\mathbf{r}^e = A^e[\mathbf{B}_m^T, \mathbf{B}_b^T] \begin{bmatrix} \mathbf{N} \\ \mathbf{M} \end{bmatrix} - \int_A \mathbf{L}^T \mathbf{f} \, dA \quad (19)$$

where A^e is the element area, $\mathbf{L}$ is the shape function matrix and $\mathbf{f}$ is the uniformly distributed loading vector.

The linear constitutive behavior of Eqs. (14) and (16) is only valid for initially flat shells and small strains. For large strains or non - linear constitutive models a numerical integration across the thickness is performed as detailed in [10].

3. Solution strategy

An adequate solution strategy is crucial for problems that present instabilities or negative stiffness along parts or the entire equilibrium path. Flat membranes under shear present typically a stable symmetrical bifurcation point with a strongly non - linear post-critical behavior where the number of wrinkles increases with shear. The final state also includes two boundary zones in a slack state. Fabric drape undergoes large displacements, rotations and shear strains. Simulations must deal with large free-hanging lengths, extensive folds and fabric-to-solid contact. The strategy adopted here is a sort of dynamic relaxation and the main aspects are:

- An explicit time integrator is used [Box 1]. This approach allows to easily dealing with the important instabilities associated to wrinkling.

- A strong damping is introduced to obtain a pseudo - static solution
- When necessary, self-weight (or an initial velocity field) is introduced to trigger normal displacements, or to avoid a completely slack state over parts of the membrane.

4. Examples

The formulation presented has been implemented in the explicit dynamic finite element code STAMPACK used for the computations [19]. Results have been obtained with an Intel Core Duo E6550 (2.33 GHz) CPU under Windows XP operating system. As no stiffness matrices are necessary the memory requirements are quite low. CPU times are given for reference to show the excellent performance of the proposed strategy.

4.1. Square thin film under in-plane shear

This example has been previously analyzed in [23] using a commercial code [24]. Experimental data is also available [25]. The problem consists of a square membrane (see Fig. 2) with side $a = 229$ mm made of a thin film of Mylar with thickness $h = 0.0762$ mm and density $\delta = 1000$ kg/m^3. The Mylar mechanical properties are $E = 3790$ N/mm^2 and $v = 0.38$. The top and bottom edges are clamped and the lateral edges are free. The top edge is subjected to a uniform horizontal displacement $\Delta = 1$ mm along the edge.

The geometry, material properties and boundary conditions have been taken from [23]. The action of gravity has been included along the (negative) z-direction with two aims: (1) to avoid the inclusion of geometric imperfections (or initial velocities) and (2) to induce negative displacements on the free edges.

Three uniform structured meshes were considered with 26×26, 51×51 and 101×101 nodes with 1250, 5000 and
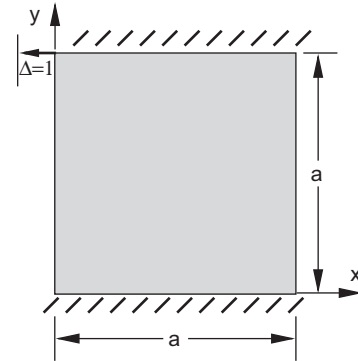

Fig. 2. Square thin film under in-plane shear.

Box 1–Explicit time integration scheme [22]

At each time step n where displacements have been computed:
1. Compute the internal forces $\mathbf{r}^n$.
2. Compute the accelerations at time t_n: $\quad \ddot{\mathbf{u}}^n = \mathbf{M}_d^{-1}[\mathbf{r}^n - \mathbf{C}_d \dot{\mathbf{u}}^{n-1/2}]$
   where $\mathbf{M}_d$ is the diagonal (lumped) matrix and $\mathbf{C}_d$ is a damping matrix (taken proportional to $\mathbf{M}_d$).
3. Compute the velocities at time $t_{n+1/2} = t_n + \frac{1}{2}\Delta t$: $\quad \dot{\mathbf{u}}^{n+1/2} = \dot{\mathbf{u}}^{n-1/2} + \ddot{\mathbf{u}}^n \Delta t$
4. Compute the displacements at time $t_{n+1} = t_n + \Delta t$: $\quad \mathbf{u}^{n+1} = \mathbf{u}^n + \dot{\mathbf{u}}^{n+1/2} \Delta t$
5. Update the shell geometry
6. Check frictional contact conditions

20 000 EBST elements, respectively. In the sequel these meshes will be referenced as mesh 25, 50 and 100, associated to the number of subdivisions along each side.

Fig. 4 plots the out-of-plane displacements for the coarsest mesh 25 for the two possible mesh orientations (see Fig. 3). The plot on the left corresponds with the tensile orientation for the present
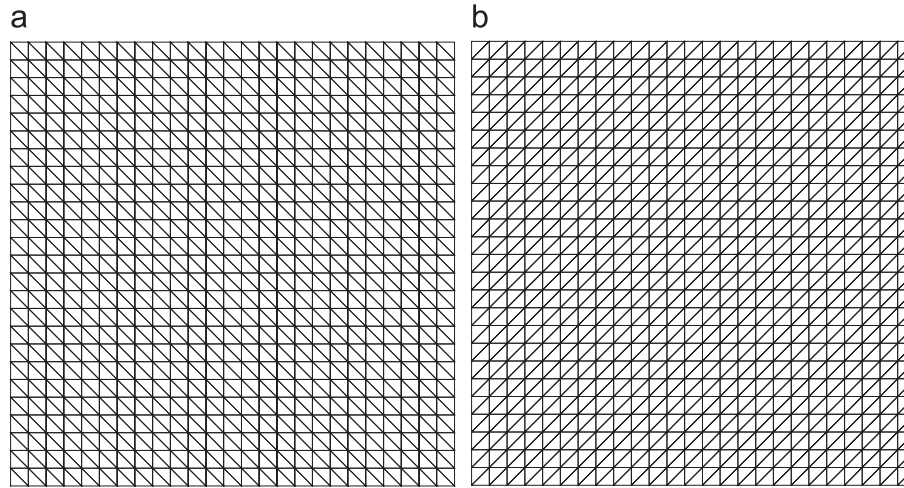

Fig. 3. Square thin film under in-plane shear. Possible orientations of the 26×26 mesh (coarsest mesh): (a) along tensile orientation and (b) along the compressed diagonal.
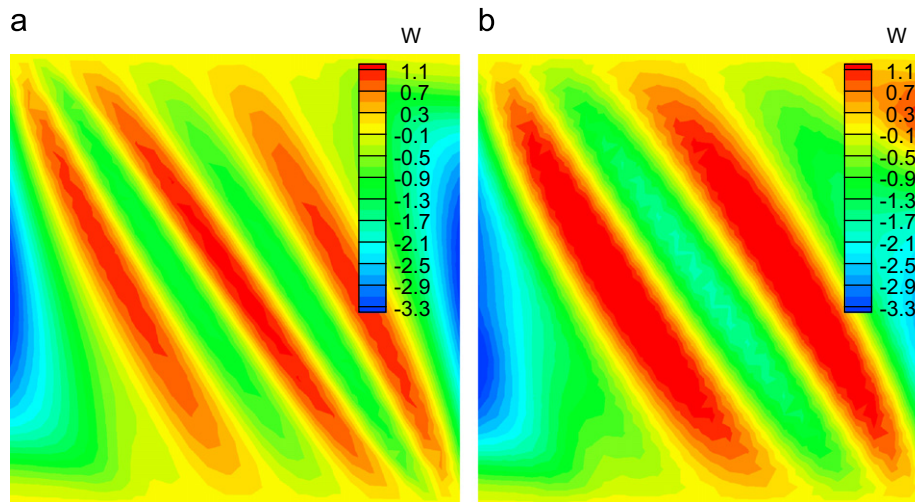
Fig. 4. Square thin film under in-plane shear. Out-of-plane displacement for the coarsest mesh: (a) tensile orientation and (b) compression orientation.
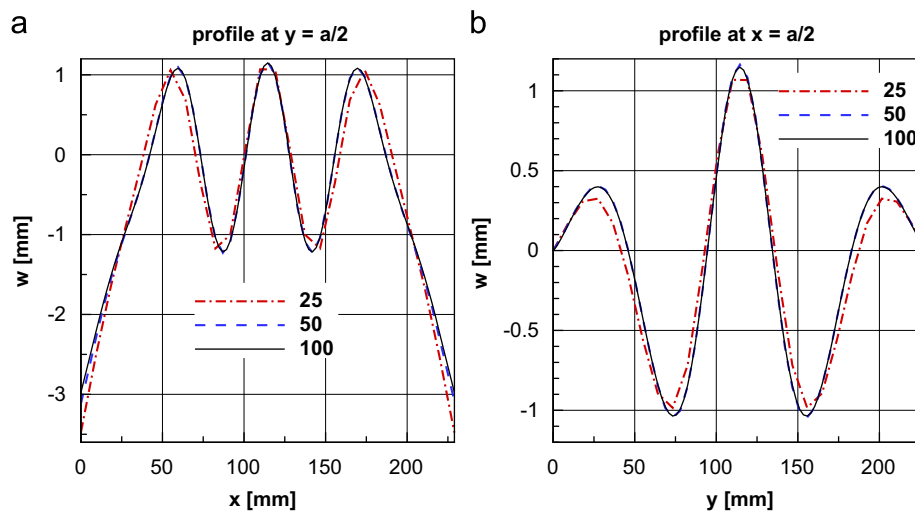
Fig. 5. Square thin film under in-plane shear. Out-of-plane displacement profiles along the square center: (a) $y = a$ and (b) $x = a/2$.

problem, where each square is divided in two triangles along the tensile diagonal. Clearly this mesh orientation behaves more flexible and converges faster to the solution. For that reason only this orientation will be considered in the sequel. It is important to remark that the meshes with the orientation along the compressed diagonal also converge to the solution but for finer meshes.

Fig. 5 plots two out-of-plane displacement profiles along the center of the square in both Cartesian directions. The plot on the left corresponds to $y=114.5$ [mm] while the plot on the right corresponds to $x=114.5$ [mm]. The results for the three meshes defined above are included. These deformed configurations are similar to the experimental evidence [25] and also coincide with the numerical results presented in Ref. [23] obtained with a commercial code [24] using the S4R5 quadrilateral element. In that work mesh 100 was used and reported as the minimum acceptable mesh according to their convergence studies. From the plots in Fig. 5 it can be seen that meshes 50 and 100 give almost identical results, while the differences with mesh 25 are quite small. For practical purposes the coarsest mesh seems to be enough to obtain the details of the final deformed shape. This is due to the (assumed strain) improved membrane behavior of the EBST element that is notably superior to the bi-linear quadrilateral.

Finally, Fig. 6 shows the deformed configurations for the coarse and fine meshes used. A magnification factor of five for
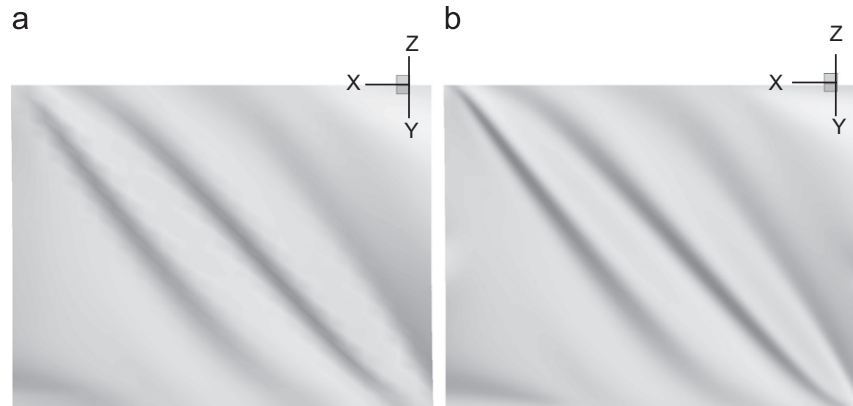

Fig. 6. Square thin film under in-plane shear. Perspective view of the deformed configuration (5X in Z): (a) coarse mesh 25 and (b) fine mesh 100.
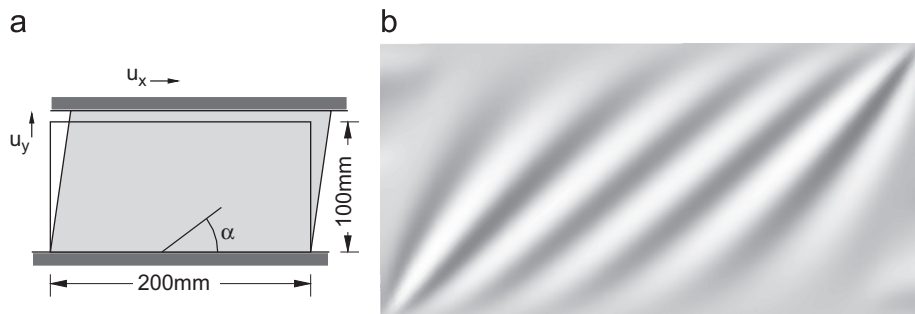

Fig. 7. Anisotropic rectangular membrane: (a) geometry and (b) final deformed configuration (2X for Z).
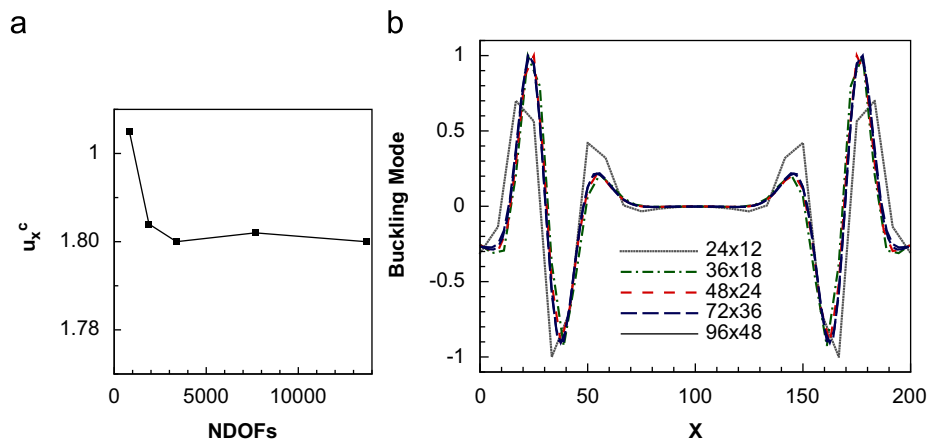

Fig. 8. Orthotropic rectangular membrane: (a) critical displacement vs. number of DOFs and (b) profile of critical mode for the different meshes.

the normal displacement has been chosen. It can be observed the excellent results obtained with the coarsest mesh that involves only 1872 DOFs compared with the mesh used in [23] that has over 50.000 DOFs. The CPU times for the simulations are 32, 260 and 2080 s, respectively, for each of the three meshes considered.

4.2. Anisotropic rectangular membrane under shear

This example has been studied in [25] using solid elements as a reference solution to assess an algorithm for wrinkling prediction. Fig. 7a shows the geometry of the rectangular domain. The membrane is clamped at the longest sides and free at the shortest side.

The membrane is first stretched in the shortest direction ($u_y=1$ mm) and is then sheared moving the upper edge ($u_x=10$ mm). The membrane thickness is $h=0.2$ mm and the constituent material has orthotropic properties. The linear relation (plane stress) between stresses and strain (in principal

directions of the material) is given by:

$$\begin{bmatrix} \sigma_{11} \\ \sigma_{22} \\ \sigma_{12} \end{bmatrix} = \begin{bmatrix} 112.375 & 25.480 & 0.000 \\ 25.480 & 112.375 & 0.000 \\ 0.000 & 0.000 & 11.32 \end{bmatrix} \begin{bmatrix} \varepsilon_{11} \\ \varepsilon_{22} \\ 2\varepsilon_{12} \end{bmatrix} \text{MPa} \qquad (20)$$

For the present example, the angle between the global $x-y$ direction and the orthotropic principal direction is $\alpha=30°$. Self-weight (density $\delta=1000$ kg/m³) is assumed to act along the negative direction of the global z-axis.

Five different structured meshes with the same coordinate increment in both in-plane directions and with the triangles oriented along the tensile diagonal have been considered. The meshes are identified with the number of divisions per side (e.g. 24×12).

For reference (and not as part of the strategy proposed) an initial buckling analysis is performed (with an implicit code) to compute the displacement u_x for which wrinkling starts and the buckling mode appears. Fig. 8a plots the critical displacement u_x as a function of the discretization (number of DOFs). Fig. 8b shows the profiles of the buckling mode along the x direction at the coordinate $y=50$ mm for the different meshes considered. Clearly, the coarsest mesh is insufficient but the rest give similar profiles, showing the excellent convergence properties of the EBST element.

Fig. 9 shows the displacement profiles for the final shear displacement of $u_x=10$ mm. Note that in contrast with the buckling mode, where the displacements are almost null at the central part (Fig. 8), the whole membrane is wrinkled for this level of shear. The displacements corresponding to the two finest meshes are practically coincident and have minor differences near the free edges. Fig. 7b shows a view of the final deformation. The vertical displacements have been amplified twice for visualization purposes. The results shown are similar to those presented in [2] where the number of DOFs used is one order of magnitude higher (120 000 DOFs).

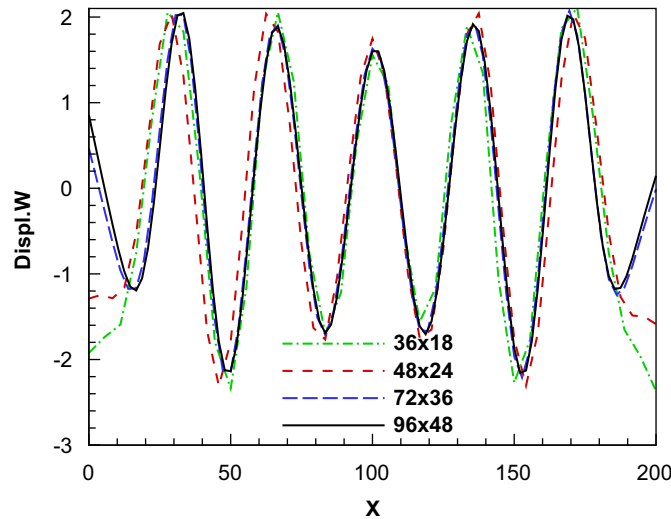For the 72×36 mesh the CPU time amounted to almost 4 min.

4.3. Circular fabric draped over a circular pedestal

This example simulates a circular (diameter 25.4 cm) wool fabric laid over a circular (diameter 12.7 cm) pedestal. Owing to symmetry, only a quarter of the fabric is modeled with the symmetric boundary conditions prescribed. To simplify the simulations the nodes on the pedestal are all assumed fixed (contact could have been considered
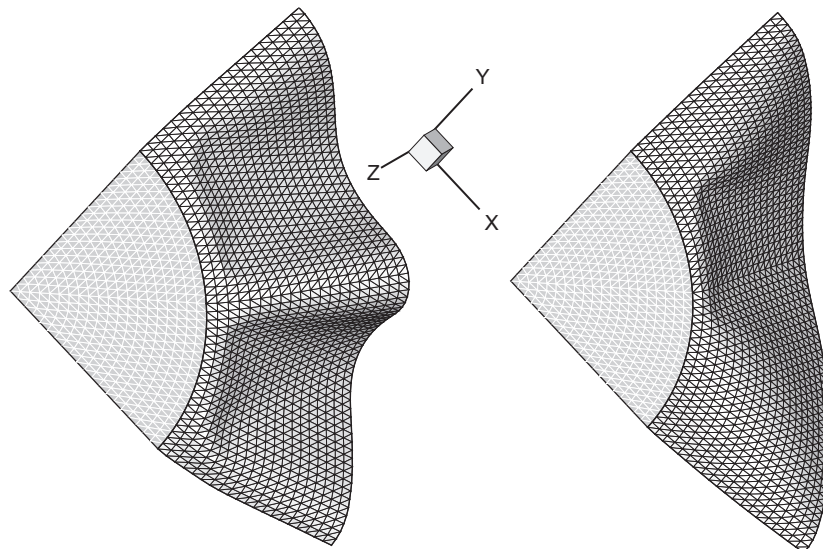

Fig. 9. Anisotropic rectangular membrane. Deformed configuration for $u_x=10$ mm. Displacement profiles for different meshes.

Fig. 10. Circular fabric over a circular pedestal. Final deformed configurations for two different loading histories.
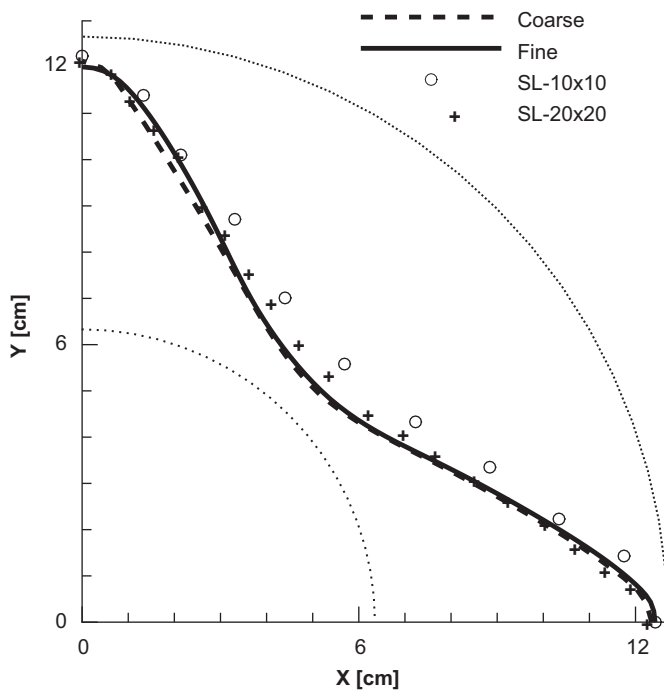
Fig. 11. Circular fabric over a circular pedestal. Comparison of results.

instead). Gravity is the only action. The mechanical properties of the fabric are those indicated in Ref. [26] and are defined by

$$
\begin{bmatrix} N_{xx} = 1096\varepsilon_{xx} \\ N_{yy} = 744.3\varepsilon_{yy} \\ N_{xy} = 40.96\gamma_{xy} \end{bmatrix} [\text{N/m}] \quad \begin{bmatrix} M_{xx} = 8142 \times 10^{-9}\kappa_{xx} \\ M_{yy} = 6174 \times 10^{-9}\kappa_{yy} \\ M_{xy} = 0 \end{bmatrix} [\text{Nm/m}]
$$

with thickness $t = 0.593$ mm and surface density $\delta = 0.1898$ kg/m^2. This type of problems does not have a unique solution and is strongly dependent on the initial conditions or the loading history. Fig. 10 shows two possible final configurations for two slightly different loading histories. The simulation corresponding to the figure on the right includes a point load at the center of the external circle directed downwards. This load begins with value 0.002 N and goes down linearly to zero at half the simulation time. Note that as only one quarter of the circle has been discretized, the number of possible solutions might have been reduced. However, due to the orthotropic properties of the material this does not seem very probable. Besides the final deformed configuration with one (right) and two (left) waves shown in Fig. 10 there exist other possible solutions with different number of waves, for example a final configuration with 1.5 waves can be easily obtained. Note that a higher number of waves implies a larger bending energy and the configuration may be rather unstable.

Two meshes were considered to assess convergence, a coarse mesh with 600 regular triangular elements and a fine mesh with
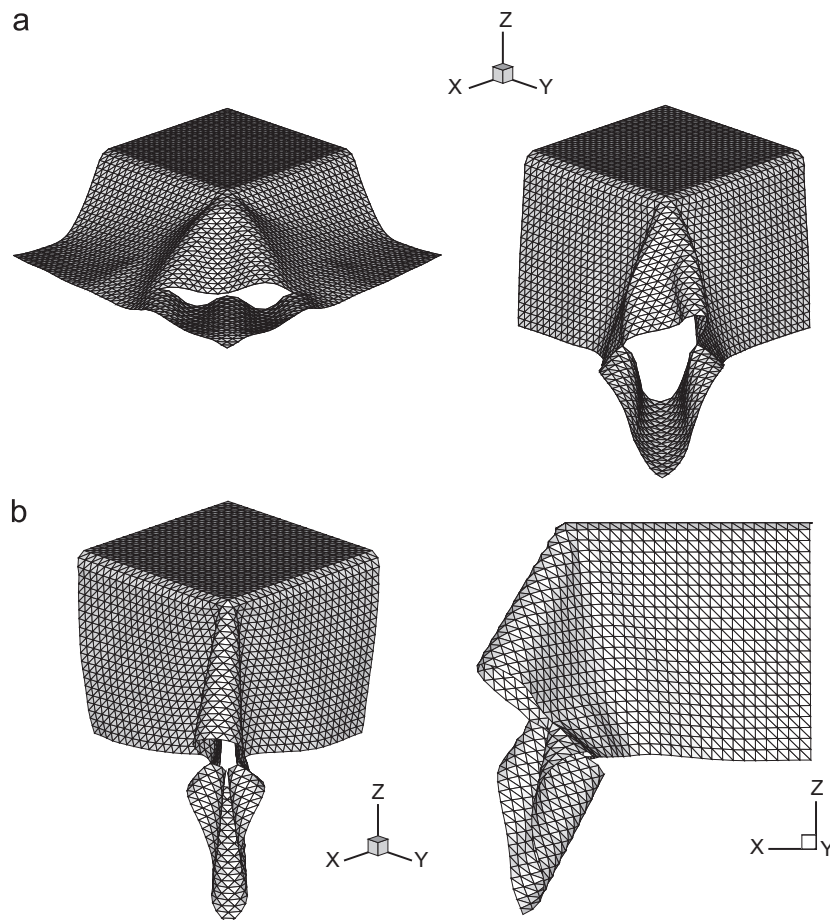

Fig. 12. Square fabric over a pedestal: (a) intermediate configurations and (b) final configuration.

2400 triangular elements (as shown in Fig. 10). The first mesh is intermediate from the two meshes used in the reference with 100 and 400 quadrilaterals equivalent to 200 and 800 triangles, respectively. Results obtained with both meshes are almost identical and compare well with the numerical results presented in [26] (indicated in Fig. 11 as "SL").

4.4. Square fabric over a square pedestal

This example, also taken also from Ref. [26], is a square (side 80 cm) wool fabric over a square (side 40 cm) pedestal. Owing to symmetry, only a quarter of the fabric is modeled with the symmetric boundary conditions prescribed. The same material properties as in the previous example were used. The nodes on the pedestal are all fixed. The fabric has an internal cut at 45° that requires a special meshing strategy when using quadrilaterals but is straightforward when using triangles. Gravity is again the only action. The results shown in Fig. 12b agree with those in [26] where numerical and experimental results are presented. The time needed to complete the simulation was 143 s. Fig. 12a shows two intermediate configurations before the fabric stops moving.

5. Conclusions

The enhanced membrane behavior of the rotation-free EBST element is crucial to obtain accurate solutions with rather coarse meshes. Two advantages of the shell triangle used (superior to any bi-linear quad) are that in its explicit form it can be used in contact problems without major problems and that it adapts easily to complex geometries.

Explicit integrators also do not require special strategies to deal with the low bending stiffness and the strong instabilities of membranes. This has important consequences for the analyst who does not need to devote time for finding the adequate strategy (buckling mode imperfection or adequate continuation parameters) necessary to arrive to the final correct result.

Other successful application of the rotation-free EBST triangle to the analysis of membranes can be found in [10,22,15,14].

References

[1] D. Steigmann, Tension-field theory, Proceedings of the Royal Society of London: Series A Mathematical, Physical Science 429 (1990) 141–173.
[2] T. Raible, K. Tegeler, S. Löhnert, P. Wriggers, Development of a wrinkling algorithm for orthotropic membrane materials, Computer Methods in Applied Mechanics and Engineering 194 (2005) 2550–2568.
[3] T. Akita, K. Nakashino, C. Natori, P.K. C, A simple computer implementation of membrane wrinkle behaviour via a projection technique, International Journal for Numerical Methods in Engineering 71 (2007) 1231–1259.
[4] A. Jarasjarungkiat, R. Wüchner, K. Bletzinger, Efficient sub-grid scale modeling of membrane wrinkling by a projection method, Computer Methods in Applied Mechanics and Engineering 198 (2009) 1097–1116.
[5] M. Pagitz, M. Abdalla, Simulation of tension fields with in-plane rotational degrees of freedom, Computational Mechanics 46 (2010) 747–757.
[6] J. Mosler, F. Cirak, A variational formulation for finite deformation wrinkling analysis of inelastic membranes, Computer Methods in Applied Mechanics and Engineering 198 (2009) 2087–2098.
[7] K. Weinberg, P. Neff, A geometrically exact thin membrane model investigation of large deformations and wrinkling, International Journal for Numerical Methods in Engineering 74 (2008) 871–893.
[8] E. Ramm, W. Wall, Shell structures—a sensitive interrelation between physics and numerics, International Journal for Numerical Methods in Engineering 60 (2005) 381–427.
[9] E. Oñate, F. Zárate, Rotation-free plate and shell triangles, International Journal for Numerical Methods in Engineering 47 (2000) 557–603.
[10] F. Flores, E. Oñate, Improvements in the membrane behaviour of the three node rotation-free BST shell triangle using an assumed strain approach, Computer Methods in Applied Mechanics and Engineering 194 (2005) 907–932.
[11] F. Sabourin, M. Brunet, Detailed formulation of the rotation-free triangular element "s3" for general purpose shell analysis, Engineering Computations 23 (2006) 469–502.
[12] J. Linhard, R. Wüchner, K.-U. Bletzinger, "Upgrading" membranes to shells—the CEG rotation free shell element and its application in structural analysis, Finite Elements in Analysis and Design 44 (2007) 63–74.
[13] F. Flores, E. Oñate, A rotation-free shell triangle for the analysis of kinked and branching shells, International Journal for Numerical Methods in Engineering 69 (2007) 1521–1551.
[14] J. Valdés, J. Miquel, E. Oñate, Nonlinear finite element analysis of orthotropic and prestressed membrane structures, Finite Element in Analysis and Design 45 (2009) 395–405.
[15] J. Valdés, E. Oñate, Orthotropic rotation-free basic thin shell triangle, Computational Mechanics 44 (2009) 363–375.
[16] N. Hamila, P. Boisse, F. Sabourin, M. Brunet, A semi-discrete shell finite element for textile composite reinforcement forming simulation, International Journal for Numerical Methods in Engineering 79 (2009) 1443–1466.
[17] F. Cirak, M. Ortiz, P. Schroeder, Subdivision surfaces: a new paradigm for thin-shell finite-element analysis, International Journal for Numerical Methods in Engineering 47 (2000) 2039–2072.
[18] N. Dung, G. Wells, Geometrically nonlinear formulation for thin shells without rotation degrees of freedom, Computer Methods in Applied Mechanics and Engineering 197 (2008) 2778–2788.
[19] STAMPACK, A general finite element system for sheet stamping and forming problems, v7.0.0, Quantech ATZ, Barcelona, España, 2010 〈www.quantech.es〉.
[20] M. Barnes, Form-finding and analysis of prestressed nets and membranes, Computers and Structures 30 (1988) 685–695.
[21] E. Haseganu, D. Steigmann, Analysis of partly wrinkled membranes by the method of dynamic relaxation, Computational Mechanics 14 (1994) 596–614.
[22] E. Oñate, F. Flores, Advances in the formulation of the rotation-free basic shell triangle, Computer Methods in Applied Mechanics and Engineering 194 (2005) 2406–2443.
[23] A. Tessler, D. Sleight, J. Wang, Effective modeling and nonlinear shell analysis of thin membranes exhibiting structural wrinkling, AIAA Journal of Spacecrafts and Rockets 42 (2005) 287–298.
[24] ABAQUS/Standard, User's Manual, version 6.3.1, Hibbit, Karlson and Sorensen Inc., Pawtucket, EE.UU, 2002 〈www.abaqus.com〉.
[25] J. Leifer, J. Black, W. Belvin, V. Behun, Evaluation of shear compliant boarders for wrinkle reduction in thin film membrane structures, in: Forty Fourth AIAA/ASME/ASCE/AHS/ASC Structures, Structural Dynamics and Materials Conference, Norfolk, Virginia, USA, 2003, pp. 5324–5330.
[26] K. Sze, X. Liu, Fabric drape simulation by solid-shell finite element method, Finite Elements in Analysis and Design 43 (2007) 819–838.